ISSN 1349-1113
JAXA-RR-08-006E

JAXA Research and Development Report

Numerical Analysis for Main-Rotor/Tail-Rotor Interaction of Helicopter

Choongmo YANG, Takashi AOYAMA,

Natsuki KONDO and Shigeru SAITO

March 2009

Japan Aerospace Exploration Agency

Numerical Analysis for Main-Rotor/Tail-Rotor Interaction of Helicopter*

Choongmo YANG[*1], Takashi AOYAMA[*1],
Natsuki KONDO[*2] and Shigeru SAITO[*3]

ヘリコプタのメインロータとテイルロータの干渉に関する数値解析*

梁　忠模[*1]，青山　剛史[*1]，近藤　夏樹[*2]，齊藤　茂[*3]

ABSTRACT

A simulation method for full helicopter configuration is constructed by combining an unsteady Euler code and an aeroacoustic code based on the Ffowcs-Williams and Hawkings formulation. The flow field and helicopter noise are calculated using a moving overlapped grid system, and the mutual effect of main rotor and tail rotor are studied for the helicopter in hover or forward flight. In the hovering flight calculation, the tip vortex of the tail rotor is dragged by the induced flow of the main rotor, and the detailed phenomena of the flow pattern are captured well. In a forward-flight calculation, noises from the main rotor and tail rotor are predicted to understand the tail rotor noise for both self noise and the interaction noise with the main-rotor wake. Comparison of noise magnitude shows that the relative importance of tail rotor noise with respect to the main rotor noise according to the flight conditions.

Keywords: BVI Noise, Main-Rotor/Tail-Rotor Interaction, CFD, Overlapped Grid System

NOMENCLATURE

c: chord length of main rotor blade
c_{TR}: chord length of tail rotor blade
r: radius of noise hemisphere
R: radius of main rotor
ψ: azimuth angle of noise hemisphere
φ: elevation angle of noise hemisphere
θ_T: angles of attack of tail rotor

1. INTRODUCTION

There are several noise sources in helicopters as shown in Fig. 1. Among these, noises from the main rotor and tail rotor can be relatively annoying to an observer on the ground, and are of interest in aerodynamics and aeroacoustics. Figure 2[1)] shows the comparison of sound pressure from helicopter for one revolution including various noise sources. Due to the size difference, isolated tail-rotor noise is known to be less important than the much louder main-rotor noise. Also, when main-rotor noise such as HSI (High Speed Impulsive) noise and BVI (Blade Vortex Interaction) noise occurs, these become dominant over other noises. However, in other flight condition, when these strong noises get fainter, noise from the tail rotor can be comparatively strong, causing annoyance and early detection.[2)]

Tail-rotor noise consists of thickness, loading, and interaction noises. The interaction noises come from (1) the interactions with the tip vortex generated by the tail rotor itself (self-interaction), (2) interactions with the tip vortex generated by the main rotor, and (3) interactions with wakes of the main rotor, hub, and fuselage. Although sufficient research to understand and reduce tail-rotor noise has not been conducted due to complicated operating

* Received 10 February, 2009（平成 21 年 2 月 10 日受付）
*1 Numerical Analysis Group, Aerospace Research and Development Directorate（研究開発本部　数値解析グループ）
*2 NIPPI, Inc.（日本飛行機株式会社）
*3 Operation and Safety Technology Team, Aviation Program Group（航空プログラムグループ　運航・安全技術チーム）

conditions and aerodynamic environment, some research offers good guidance for tail-rotor analysis. Chou[3] showed that the interaction with the main-rotor turbulent wake is an important source of tail-rotor broadband noise. Martin[4] presented acoustic data from a model-scale main-rotor and tail-rotor experiment at different directivity locations. Balch[5,6] conducted experimental studies on the interaction in hover to explain the overall effects of the tail rotor. Leverton *et al.*[7] showed tip vortex trajectories for the main rotor during hover and in forward flight in Fig. 3. The effect of tip vortex on the tail rotor by many interactions depends on the helicopter flight condition and the location/operating condition of the tail rotor. In the CFD research field, the need for huge computing resources has blocked simultaneous simulation of the main rotor and tail rotor. Most studies are related to the isolated tail rotor, and focus on loading or thickness noise,[8] or the interaction characteristics of the tail rotor are simplified for limited cases, such as using an isolated vortex.[9,10] As the need to build quieter helicopters increases, it is more necessary to understand the physics of tail-rotor noise, including interaction characteristics.

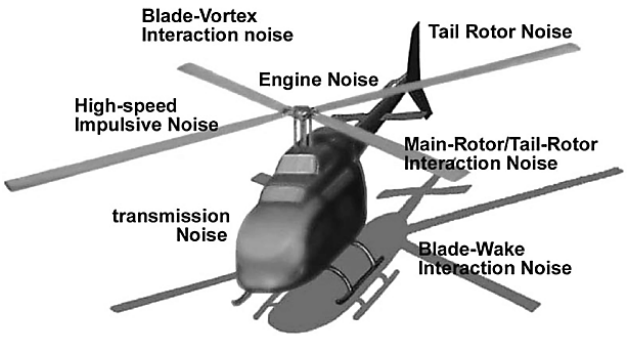

Fig. 1 Diagram of noise sources in helicopter.

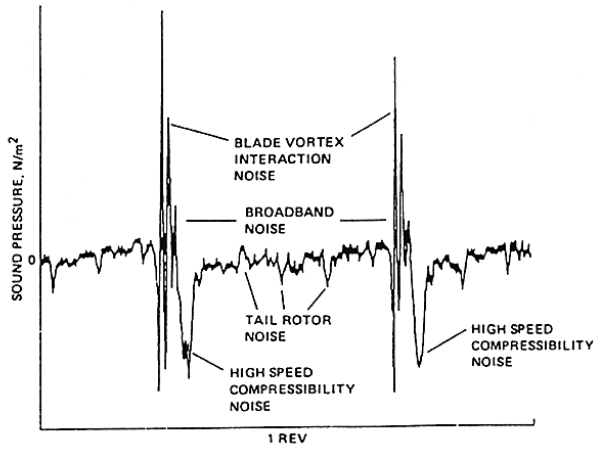

Fig. 2 Sound pressure of various helicopter noises for one revolution.

We have conducted research to construct a CFD method for full helicopter simulation, including main parts, such as main rotor, tail rotor, and fuselage, based on our previous research.[11,12] This paper focuses on the interaction between the main rotor and tail rotor, and the main goal is to clarify the mutual effects between the main rotor and tail rotor for hovering and forward flight. The results show the noise from the main rotor and tail rotor, and the relative importance of tail-rotor noise is discussed for both self-interaction noise and interaction noise with the main-rotor tip vortex.

2. NUMERICAL METHODS

2.1. Overlapped grid system

A moving overlapped grid system with three different types of grid (rotor grid, inner and outer background grids) is used to simulate a complicated helicopter flow. Figure 4 shows the grid system used in the calculation. Figure 4 (a) shows a perspective view for the whole computational domain of the grid system. The inner background grid is placed around the rotor disk, and the outer background grid covers the whole computation region with a

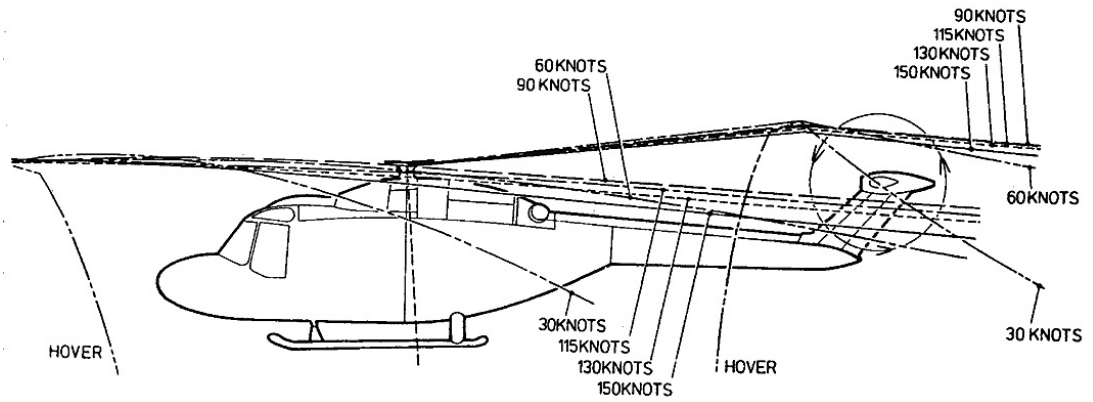

Fig. 3 Tip vortex trajectories during hover and forward flight[6].

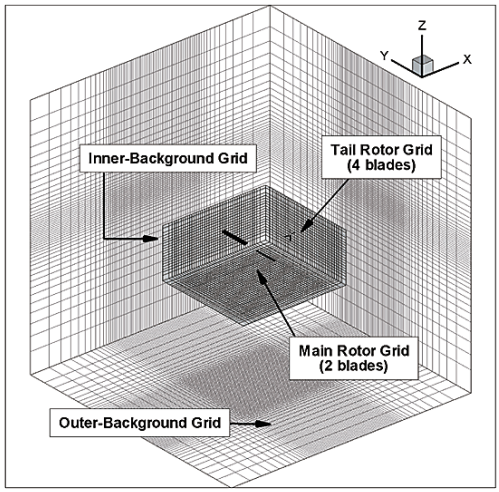

(a) overlapped grid system

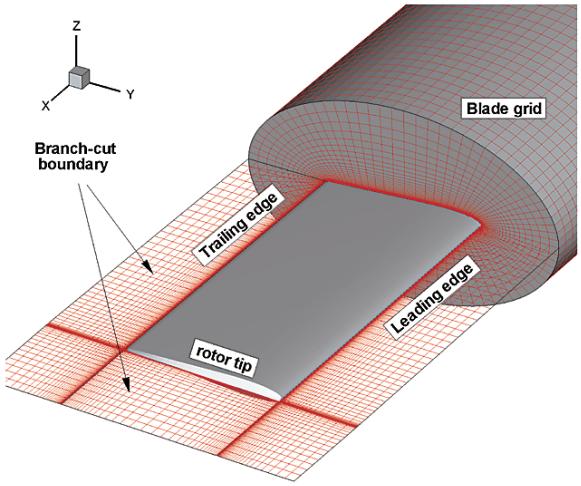

(b) Cross section of blade grid and boundary condition
Fig. 4 Perspective view of grid system.

sparse grid density. The flow data are exchanged between the inner and outer background grids, and between the rotor grid and inner-background grid. The body-fitted blade grid in O-H topology, as shown in Fig. 4 (b), moves along with the blade motion, including rotation, flapping, feathering, and lagging motions.

The geometric dimension of two background grids is shown in Fig. 5. The airfoil model of the main-rotor blade comes from AH1-OLS blade[13] (modified BHT 540), which has been used for aerodynamic and noise testing by NASA. The characteristics of an OLS rotor with a 1.916 m diameter (6.6 ft) are shown in Fig. 6. The aspect ratio of the main rotor is 9.21. Figure 7 illustrates the relative position of the tail rotor and the geometric specifications of each rotor. The tail rotor is a pusher type, producing thrust to the other side of the tail-rotor location. The airfoil model of the tail-rotor blade is NACA0012, and the angle of attack is 5° without twist angle. The radius of the tail rotor is 1/6 of the main rotor, and the aspect ratio of the tail rotor is 7.0. Table 1 shows the specification of each grid. Most of the grid is concentrated in the inner-background grid, which captures the trace of the tip vortex during several rotations. The number of grid points in the spanwise direction is increased considerably to match the grid density of the blade grid with that of the inner background grid. The grid spacing of the inner background grid corresponds to $0.1c$, where c is the chord length of the main rotor.

A 3D numerical flow solver[14] for the compressible Euler equation is used to analyze the detailed behavior of the tip vortex. The different numerical schemes are used according to the different types of grid system.

For the blade calculation, inviscid flux vectors are separated using Roe's flux difference splitting (FDS) algorithm,[15] where flux difference across a cell interface is divided into components associated with each characteristic wave with third-order accuracy using a TVD scheme. The TVD scheme is known to be good at capturing shock waves without adding artificial dissipation.

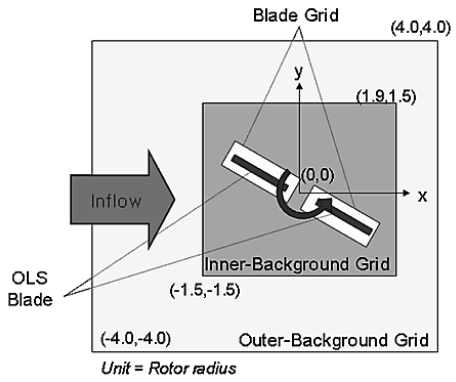

Fig. 5 Geometric dimension of computation.

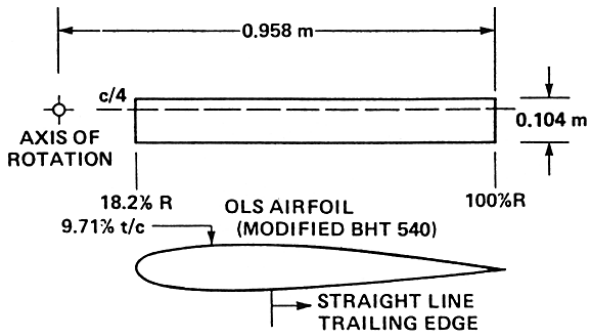

Fig. 6 Geometric dimension of OLS model rotor.

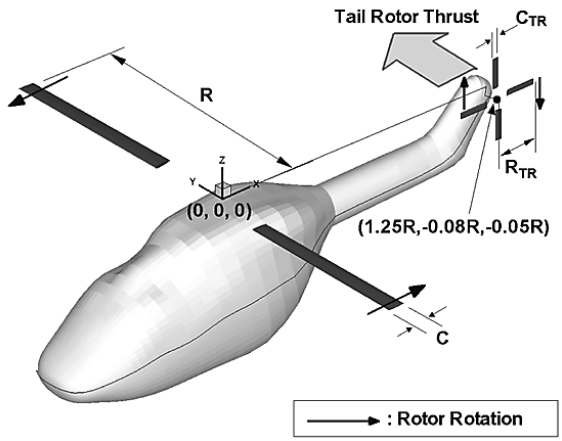

Fig. 7 Geometric dimension of main/tail rotors.

Table 1 Specification of grid system.

	Grid
Inner-background grid	(x × y × z) 450 × 400 × 80 = 14,400,000
Outer-background grid	(x × y × z) 83 × 79 × 49 = 321,293
Main-rotor grid	(chord × normal × span) × blade (77 × 20 × 70) × 2 = 215,600
Tail-rotor grid	(chord × normal × span) × blade (77 × 20 × 55) × 4 = 338,800
Total	15,275,693 points
Spacing of inner-background grid	$0.1c\ (= 0.005R)$

Since Roe's approximate Riemann solver does not have consistency with the entropy condition and thus permits physically inadmissible expansion shock, an entropy correction is applied to resolve this inconvenience. For the time integration, a first-order Euler backward scheme is used in the conventional delta form. A diagonalized ADI method with an upwind flux-split technique is used in the linearized implicit part for the discretized governing equations. A detailed derivation of the governing equation and numerical schemes is described by Aoyama *et al.*[16] To obtain the second-order accuracy of the unsteady solution in forward flight, the Newton iterative method with four iterations is used at each time step. The typical dividing number along the azimuthal direction is about 4800 per revolution, which corresponds azimuth angles about 0.075°. The unsteady calculation is started impulsively from the azimuth angle of 0°. From previous research, the starting vortex can be negligible in forward flight calculation.

For calculations over Cartesian background grids (inner- and outer-background grids), the flux difference across the cell interface is divided using a compact TVD scheme[17] to get third-order accuracy in space. Then, MUSCL cell interface value is modified to achieve fourth-order accuracy. The Simple High-resolution Upwind Scheme (SHUS)[18] is used to obtain numerical flux. SHUS is an Advection Upstream Splitting Method (AUSM)-type approximate Riemann solver and has small numerical diffusion. The four stage Runge-Kutta method is used for time integration. The free-stream condition is applied for the outer boundary of the outer-background grid.

Calculations are performed using the Central Numerical Simulation System (CeNSS), the third-generation numerical simulator of JAXA. It takes about 100 hours to obtain a fully converged solution of a rotor Euler calculation with about 15 million grid points using 36 CPUs.

2.2. Noise calculation using Ffowcs-Williams and Hawkings formulation

The prediction method for the far-field acoustic pressure is based on a combination of the CFD technique with an acoustic solver. Although direct computation can be used to get the noise solution directly from the flow calculation with CFD-based methods, this is only available in the near field despite huge computing costs. At present, the best way is coupling CFD results with the acoustic solver for far-field noise prediction.

The Ffowcs Williams and Hawkings (FW-H) equation, which is re-arranged from the acoustic analogy, is widely used and still under construction for better applications. The retarded time solution to the FW-H equation, neglecting quadruple noise, can be written in the form of Formulation 1 by Farassat[19]. To satisfy

hypothesis of the FW-H equation[20], it is known that the noise source must lay in the low speed flow, and the observer should be located outside the source region (i.e. outside the boundary layer, separation flow or wake) in order to avoid a nonlinear effect. In most calculations to compare the results with wind-tunnel experiments, the observer moves in the same direction and at the same speed as the noise source.

Rotor noise is predicted by the following procedures: 1) calculation of sound pressure of noise source, 2) acoustic prediction computation at observer position, and 3) post-processing of noise data for sound level using visualization or audible converting. The pressure distribution on the blade surface calculated by the CFD code is stored every 0.5 degrees in the azimuth-wise direction as the noise calculation input data.

3. RESULTS

3.1. Validation

Validation of the present code is performed for the main-rotor BVI condition to check the ability to capture BVI phenomena. The tail-rotor interaction consists of two interactions: self-interaction, and interaction with the main-rotor wake. Self-interaction of the tail rotor is identical to self-interaction of the main rotor except for the size and direction of the rotation axis. The interaction between the tail rotor and main-rotor wake is also similar to the main-rotor BVI or tail-rotor self-interaction except that the relative speed and size between main-rotor wake and tail-rotor wake are different. Consequently, the main-rotor BVI problem is adequate for validation of the present code for the tail-rotor calculation.

For the main-rotor BVI problem, numerical computations are performed for the realistic rotor system, which was tested in the anechoic Deutsch-Niederlaendischer Windkanal (DNW). Acoustic data have documented the BVI impulsive noise radiated from a 1/7-scale model main rotor of the AH-1 series helicopter. The dynamic blade motions such as flapping, feathering, and lagging are defined by the input data, which include first harmonic functions obtained by CAMRADII (Comprehensive Analytical Code for Rotorcraft Aerodynamics and Dynamics).[21] One test condition is chosen to evaluate the ability of our original code to predict BVI noise. The specification of the calculated rotor and operating conditions are summarized in Table 2, where the shaft tilt angles are corrected by Heyson's method.[22]

Figure 8 shows the microphone positions in the experiment, where high BVI noise can be measured. Sound pressure is calculated at these positions using blade surface pressure by the aeroacoustic code based on the FW-H formulation.

Table 2 Operating conditions.

Thrust coefficient, C_T	0.0054
Tip Mach number, M	0.664
Advance ratio, μ	0.164
Tip path plane angle	1.0°（aft.）

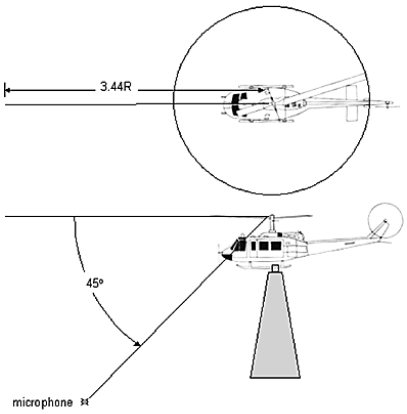

Fig. 8 Microphone position.

Figures 9 (a) and (b) show the measured and calculated time histories of sound pressure at the microphone positions shown in Fig. 7. CFD results by Strawn *et al.*[23] are shown by the gray lines. They are applied to the trim condition indicated as "Strawn" in Table 3 to obtain the acoustic signals without iteratively adjusting the trim condition to the experimental thrust value with zero rolling moments across the rotor disk. While the positive spikes observed in the experimental data (dotted lines), which are caused by interactions between blades and vortices, are not clearly captured by their method in both microphone positions, the predictions are fairly improved by the present method using the same trim condition as indicated by the thin lines. If the trim condition calculated by CAMRADII shown in Table 3 is applied to the present method, the improvement becomes more remarkable except for over-predictions of the first negative and positive peaks at Mic.3 as indicated by the black lines. Therefore, prediction of BVI noise is strongly affected by trim data.

Although the peak values show some discrepancy in magnitude, the calculation shows good agreement in peak position. There are several reasons for the discrepancies between the experimental data and our predictions, such as lack of accuracy in calculated trim condition, numerical scheme, and interpolation used in the overlapped grid method, neglect of viscosity and blade elasticity, and lack of grid resolution. However, we confirmed that our method at least successfully captures distinct spikes in BVI noise, according to the discussion here. Higher accuracy numerical schemes and very large-scale computation lead to these satisfying results, implying that calculation can pre-

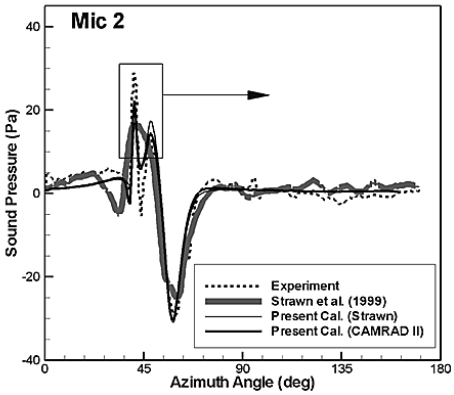

(a) at Mic. 2

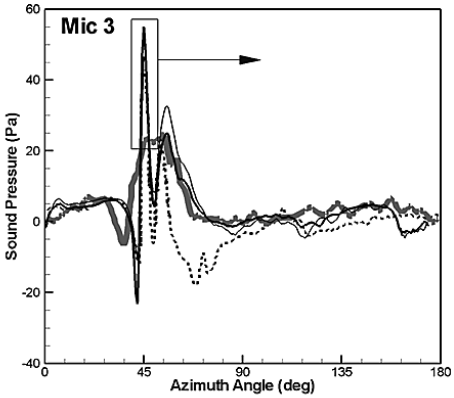

(b) at Mic. 3

Fig. 9 Comparison of sound pressure between calculation and measurement.

Table 3 Trim conditions.

	Strawn	CAMRAD II
Collective pitch angle, θ_0	6.14°	5.73°
Lateral cyclic pitch angle, θ_c	0.9°	0.97°
Longitudinal cyclic pitch angle, θ_s	1.39°	1.86°

dict BVI phenomena, which are characterized by the sound pressure peak.

3.2. Hovering flight

Hovering helicopter flight is simulated to understand the mutual effect between the main rotor and tail rotor. As a reference, flow around the main rotor only **(MR)** without tail rotor is calculated. The tail-rotor angles of attack, θ_T, are set to be 0° (non-lifting case: **TR0**) and 5° (lifting case: **TR5**). Table 4 shows the main-rotor and tail-rotor operating conditions in hovering flight.

Figure 10 shows the pressure history of the main rotor (upper) and tail rotor (lower) at one typical point on the upper surface (90% of span, 3% of chord) during one revolution of the main rotor. As shown in Fig. 10 (a), the presence of the tail rotor for **TR0** and **TR5** (solid line and dashed line) causes the disturbed

Table 4 Operating conditions in hover.

Main rotor	
Tip Mach number, M_{MR}	0.664
Advance ratio, μ	0.164
Tip path plane angle	0.0°
Collective pitch angle, θ_0	0.0°
Cyclic pitch angle, θ_c θ_s	0.0°
Tail rotor	
Tip Mach number, M_{TR}	0.664
Rotation ratio w.r.t. main rotor	6.0
Geometric ratio w.r.t. main rotor	1/6

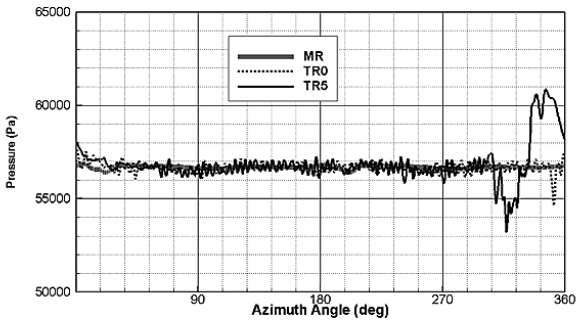

(a) Main rotor

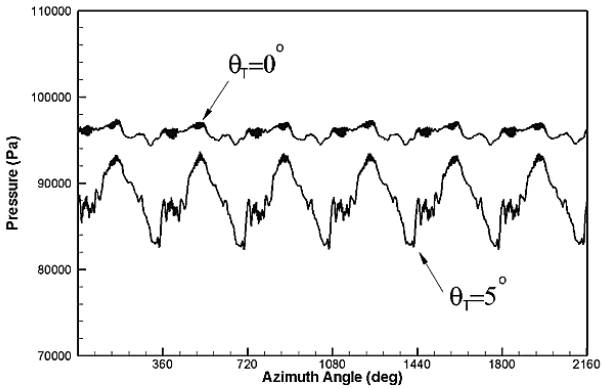

(b) Tail rotor

Fig. 10 Time history of pressure at one point on upper surface in hover.

pressure at the end of the main-rotor revolution compared to the almost flat line of **MR** (thick gray line). Comparing the pressure histories for two cases with tail rotor in Fig. 10 (b), **TR5** shows a larger oscillation than **TR0**, which is reasonable considering the flow induced by the lifting tail rotor.

The mutual effect between the main rotor and tail rotor is also shown in Fig. 11, which shows the pressure carpets and vorticity iso-surfaces at the top view of the main-rotor disk. The pressure carpets are generated by the pressure at one line (3% of chord) on the upper surface during one revolution in hovering flight. As shown by vorticity iso-surfaces, the tip vortex from a lifting tail

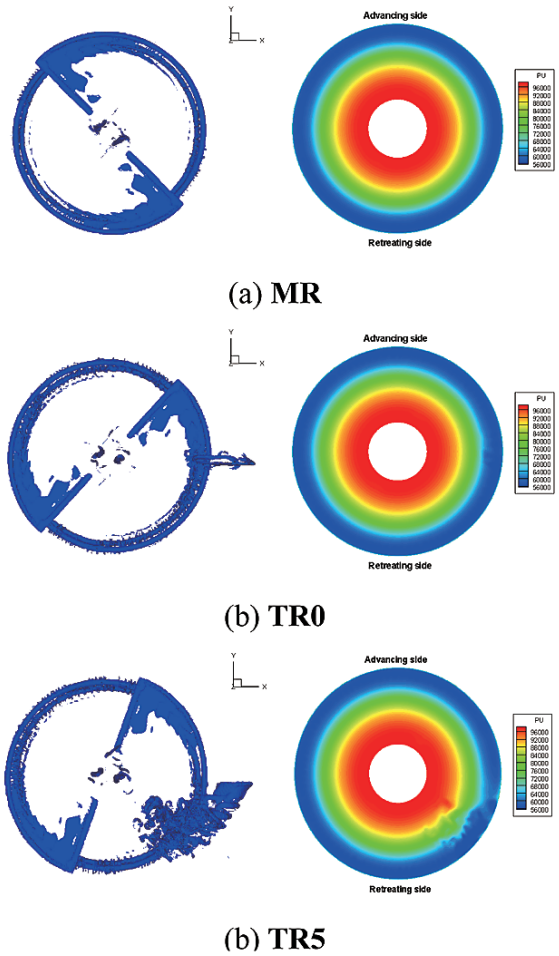

Fig. 11 Pressure carpet and vorticity iso-surface at top view of main rotor in hover.

rotor is dragged into the tip vortex of the main rotor by the induced flow of the hovering main rotor. This tip vortex from the tail rotor disturbs the main rotor around the 300 to 330˚ azimuth angle, which also appears in the previous figure of the pressure history of main rotor.

The behavior of the tip vortex from tail rotor is shown more clearly in Fig. 12, which shows the vorticity iso-surfaces and side views at three sectional planes in **TR5**. The marked circle represents the tail rotor disk, and the tip vortex of the main rotor is located at the left side of the tail rotor. The tip vortex generated from a lifting tail rotor (section A) grows to move toward the main rotor (section B) or is dragged into the main-rotor tip vortex (section C) by downwash of the main-rotor tip vortex. The vector plot in Fig. 13 shows the flow patterns of tip vortices of the tail rotor at the sectional plane (section B in Fig. 12 (b)). Figure 13 (b) shows the whole sectional plane including tip vortices from both advancing side and retreating side. The tip vortices in the advancing side show more complicated structure as shown at the zoom view in Fig. 13 (b). The tip vortex from the tail rotor is attracted to the downwash of the main-rotor tip vortex in many ways shown as dashed lines in Fig. 13. This tail-rotor vortex, which is attracted into main-rotor downwash, reversely affects the main-rotor vortex around the 300 to 330˚ azimuth angle. From the detailed CFD results, we can better understand the flow physics around the main/tail rotor at hovering.

3.3. Forward flight

Forward helicopter flight is simulated to understand the tail rotor disturbed by the tip vortex of main rotor. Owing to upwind inflow at forward helicopter flight, the tail-rotor flow information should hardly affect the main rotor. As a result, the main calculation objective is to understand the physics of the tail-rotor interaction phenomena, including the tail-rotor self-interaction and interaction between the main-rotor wake and tail rotor. Also, the noise characteristics of the main rotor and tail rotor are discussed.

Flow around the main rotor only (**MR**) without tail rotor is calculated as a reference in the same way as the hovering flight calculation. The angles of attack of tail rotor are also set to 0˚ (non-lifting case: **TR0**) and 5˚ (lifting case: **TR5**). Table 5 shows the operating conditions.

Figure 14 shows the iso-surface of vorticity in the inner-background grid at the top view for the main rotor with/without tail

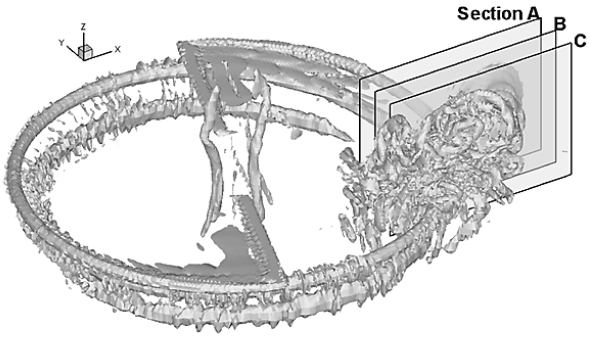

(a) Perspective view

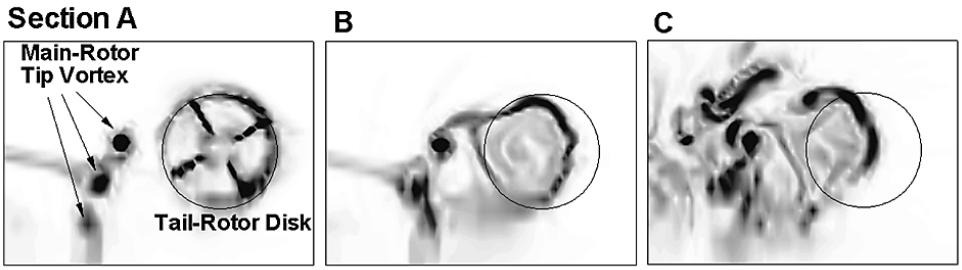

(b) Side views at sectional planes

Fig. 12 Behavior of tip vortex of tail rotor in **TR5** case at hover.

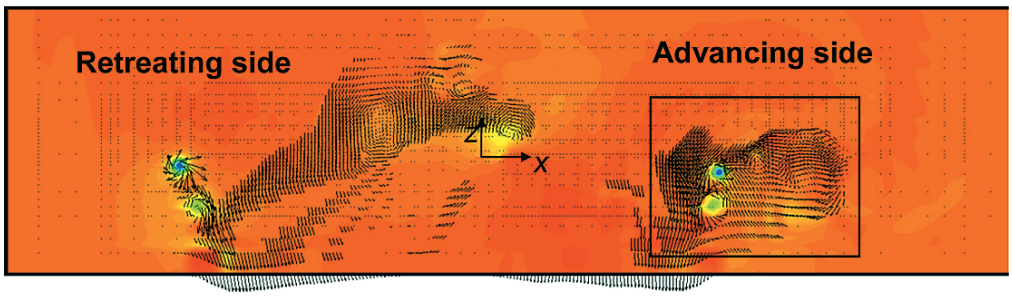

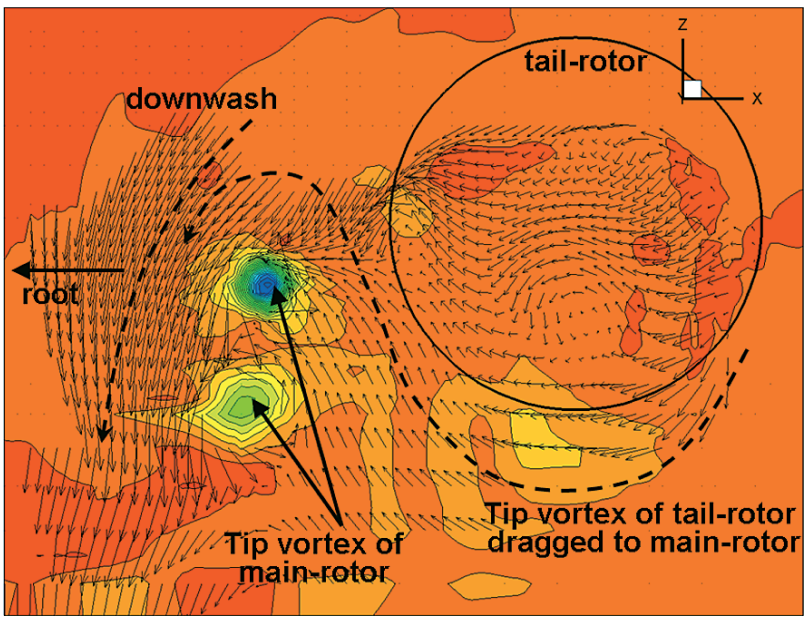

Fig. 13 Vector plot at sectional plane at hover.

Table 5 Operating conditions in forward flight.

Main rotor	
Tip Mach number, M_{MR}	0.664
Advance ratio, μ	0.164
Tip path plane angle	3.0°
Collective pitch angle, θ_0	5.2°
Cyclic pitch angle, θ_c	−1.33°
Cyclic pitch angle, θ_s	2.72°
Tail rotor	
Tip Mach number, M_{TR}	0.664
Rotation ratio w.r.t. main rotor	6.0
Geometric ratio w.r.t. main rotor	1/6

rotor. Compared to the main-rotor tip vortex in Fig. 14 (a), the vorticity iso-surfaces in Fig. 14 (b) and (c) clearly show the presence of the tail rotor. By contrast, the effect of the tail rotor on the vortex structure of main rotor seems negligible, which is expected because the main stream flows from the main rotor to the tail rotor. Detailed difference of tail rotor vortex behaviors between non-lifting case (**TR0**) and lifting case (**TR5**) is shown in Fig. 15. The non-lifting case (**TR0**) shows only the interaction among the tip vortices from the main rotor without producing tip vortex from tail rotor itself. Whereas, the lifting case (**TR5**) shows

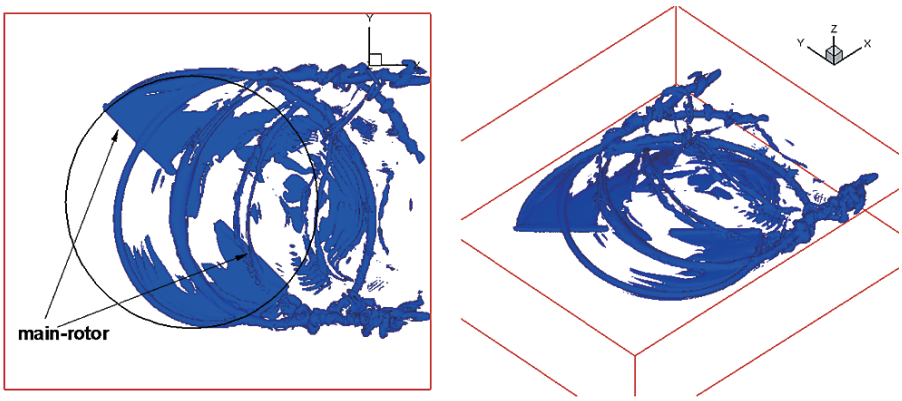

(a) **MR**

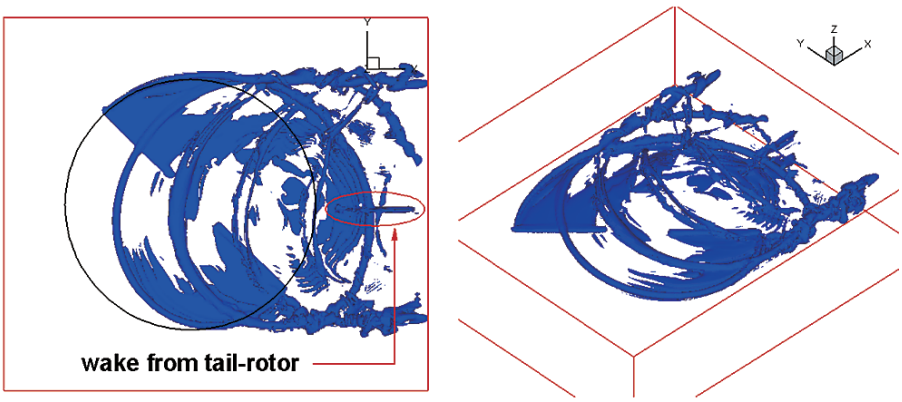

(b) **TR0**

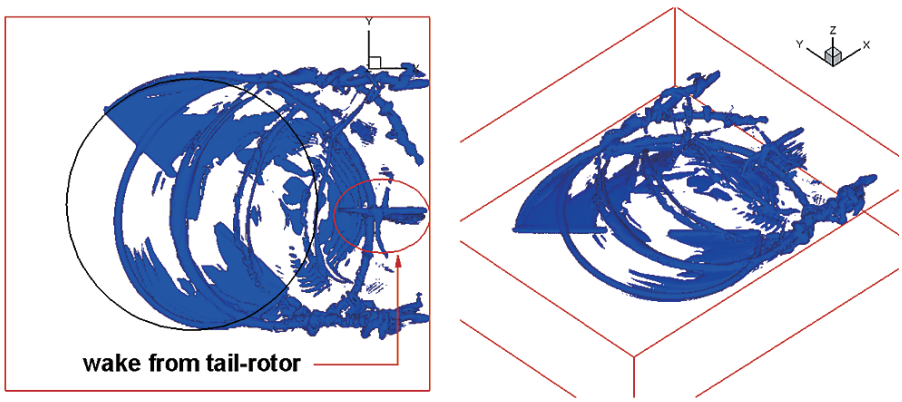

(c) **TR5**

Fig. 14 Iso-surface vorticity at top view in forward flight.

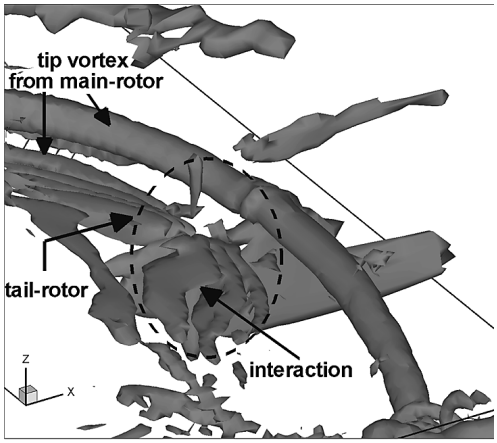

(a) **TR0**

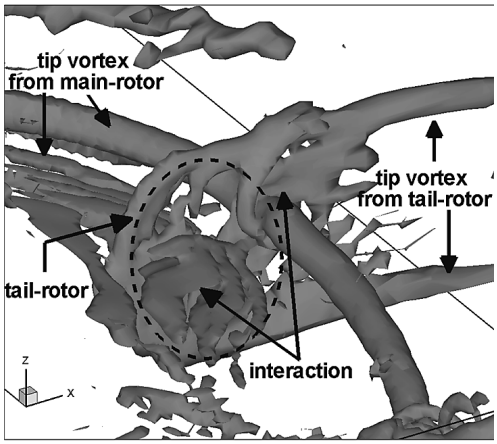

(b) **TR5**

Fig. 15 Iso-surface vorticity near tail rotor in forward flight

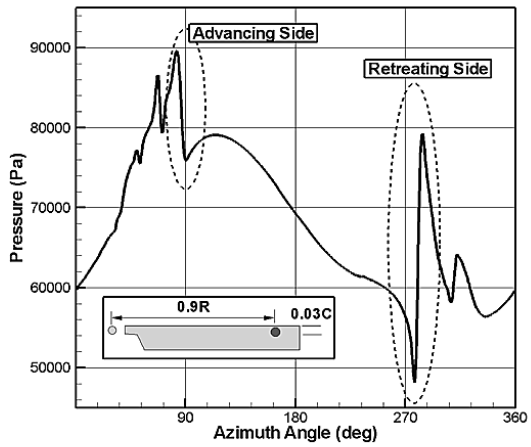

(a) Main rotor

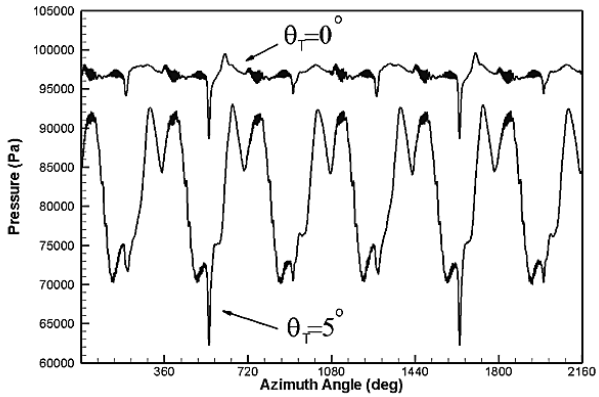

(b) Tail rotor

Fig. 16 Time history of pressure at one point on upper surface in forward flight.

strong tip vortex from tail rotor itself.

Figure 16 shows the pressure history of the main rotor and tail rotor at one typical point on the upper surface (90% of span, 3% of chord) in forward flight. As shown in Fig. 16 (a), the main rotor experiences BVI around 60˚ to 80˚ and 280˚ of azimuth angle, which appears as sudden pressure changes. As already explained, the presence of the tail rotor on the pressure history of the main rotor in forward flight seems negligible. According to the rotation ratio, which implies that the tail rotor rotates six times as fast as the main rotor during one revolution of the main rotor, six periodic patterns in pressure variation appear in Fig. 16 (b). For **TR0**, six negative peaks can be recognized easily. Among them, small peaks come from the self-interaction of the tail rotor, and large peaks come from both self-interaction and interaction with the main-rotor tip vortex. Although the non-lifting tail rotor for **TR0** should not produce a tip vortex related to self-interaction, the wake or tip vortex from the main rotor cause minute lift of the tail rotor, which produces a weak tip vortex to cause the self-interaction as a small peak in the pressure history. The effect of the interaction with the main-rotor tip vortex appears as the larger peaks around 540˚ (in the second revolution) and 1620˚ (in the fifth revolution), which happen to coincide with the self-interaction in the azimuth angle. For **TR5**, blade loading of the lifting tail rotor in forward flight produces six waves in low-frequency waves in the pressure history. The effect of the interaction with the main-rotor tip vortex appears at the same position as in **TR0**. Although the peak positions happen to be quite regular (periodic) in this flight condition, both cases note that the interval of these interaction peaks is dependent on many parameters, such as forward velocity, rotation speed of tail rotor, and number of blades in tail rotor.

Figure 17 shows the pressure carpets for the main-rotor and tail-rotor disks, which are plotted by using the pressure at one typical line (3% of chord) on the upper surface in forward flight. Because the tail rotor experiences quite a periodic pressure oscillation as shown in the previous figure, the pressure carpets during the 1st, 3rd, 4th and 6th revolution are similar, and those during the 2nd and 5th revolution are almost identical among the six tail-

rotor revolutions, which correspond to one revolution of the main rotor. From the pressure carpet during the 2nd revolution, we can easily find the interaction location with the main-rotor wake at the marked area around 165° of the tail-rotor azimuth angle, which matches the previous result.

A convenient way to understand helicopter noise directivity is by using a hemispherical surface where the center is located at the origin of the main rotor (or helicopter) as shown in Fig. 18. A point on the hemispherical surface is specified by the radius, r, the azimuth angle, ψ, and the elevation angle, φ. The azimuth angle follows the count-clockwise main-rotor rotation when viewed from above. Elevation angle is defined as a negative value downward from the tip-path plane of the main rotor. The contour values on the hemispherical surface represent the peak sound pressure radiated from the main rotor during one revolution at a distance of r/R = 1000. The peak sound pressure is obtained from the maximum sound pressure in one revolution at each point of the hemisphere in Fig. 18. To make the comparison easier, 2D planar views of hemisphere are shown in Fig. 19. Comparing three peak noise level contours, the peak positions are the same (ψ=205°, φ=-25°) regardless of the tail rotor conditions, implying that the effect of the tail rotor on the noise directivity is negligible when main-rotor BVI occurs. The difference in sound pressure level is shown in Table 6.

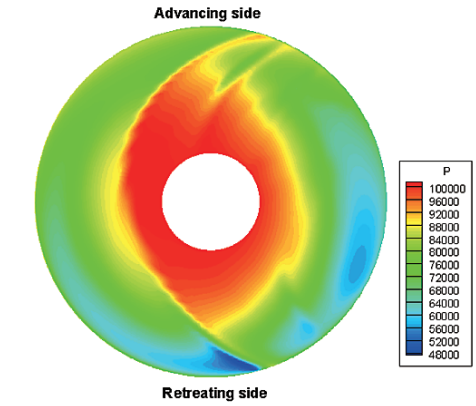

(a) Main rotor

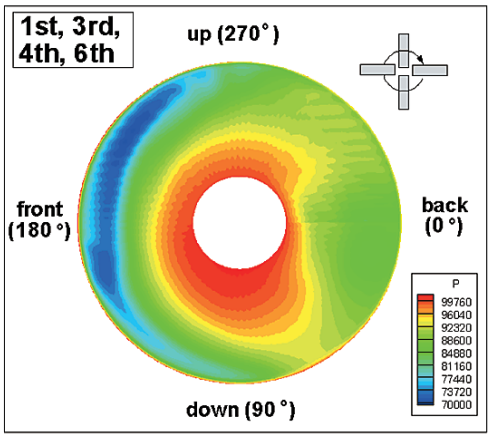

(b) Tail rotor at 1st, 3rd, 4th and 6th revolution

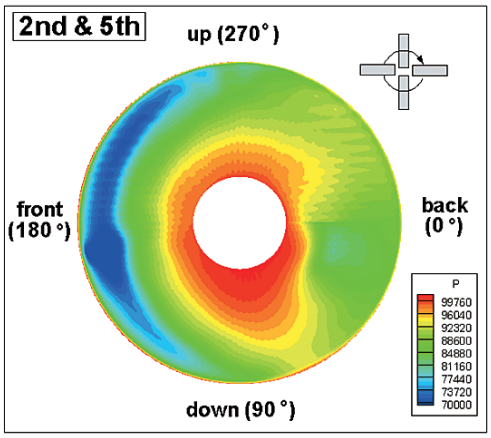

(c) Tail rotor at 2nd and 5th revolution

Fig. 17 Pressure carpets of main rotor and tail rotor during one revolution in forward flight.

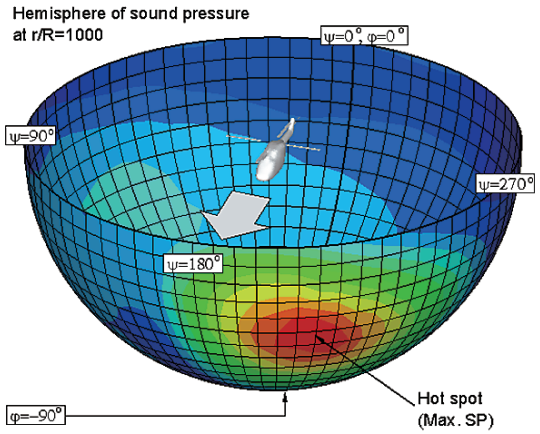

Fig. 18 Hemisphere of sound pressure at 1000R.

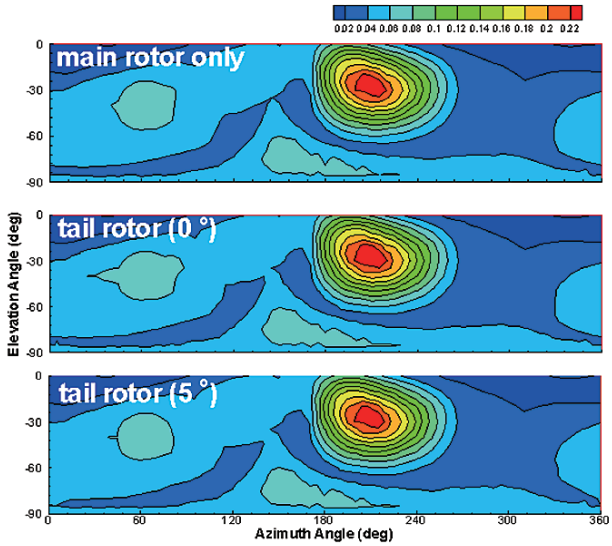

Fig. 19 Peak noise contours for BVI in forward flight.

Figure 20 shows the BVI sound pressure of the main rotor at the position of the maximum peak noise level in Fig. 18. The sound pressure waveform clearly shows distinct spikes in BVI noise. As expected, the effect of the tail rotor on the main rotor is negligible, making the three lines almost identical. The effect of the interaction on the tail rotor can be explained using the sound pressure of the tail rotor in Fig. 21. The six negative peaks in both **TR0** and **TR5** come from the tail-rotor thickness noise, and the self-interaction noise appears as six positive peaks in **TR5**.

Table 6 Peak noise positions and value.

case	ψ	φ	SP (Pa)
MR	205°	–25°	0.2380
TR0	205°	–25°	0.2394
TR5	205°	–25°	0.2365

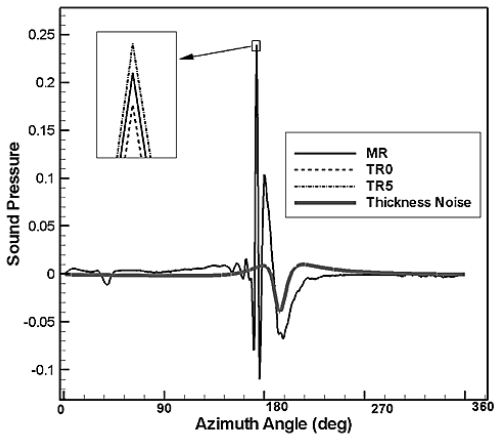

Fig. 20 BVI sound pressure of main rotor in forward flight.

Compared to **TR0**, **TR5** generates larger self-interaction noise comparable to thickness noise. For both cases, the noise from the interaction with the main-rotor wake is well captured as marked peaks at the 2nd and 5th revolution of the tail rotor. For noise magnitude, the noise from the interaction with the main-rotor tip vortex is relatively small compared to other tail-rotor noises. This can be explained from the intersection angle between the main-rotor tip vortex and tail rotor. As shown in our previous research[10], when a blade interacts with a vortex in a vertical plane perpendicular to the blade axis, only the thickness noise is remarkable in every condition, because the vortex does not induce any vertical velocity on the blade surface in this perpendicular interaction while the sudden change of vertical velocity induced by the vortex causes the BVI noise. Due to the present configuration of helicopter components and operating/flight conditions, perpendicular interaction leads to relatively small interaction noise.

Compared to main-rotor noise, which comes from main-rotor BVI, tail-rotor noise for both **TR0** and **TR5** seems small but should not be ignored. As a matter of course, when main-rotor BVI occurs, the peak noise level from the main rotor is very high compared to other noises including tail-rotor noise. However, as mentioned in the introduction, when these strong noises become fainter due to flight conditions, the tail-rotor noise can be comparatively strong. Consequently, although tail-rotor noise in the

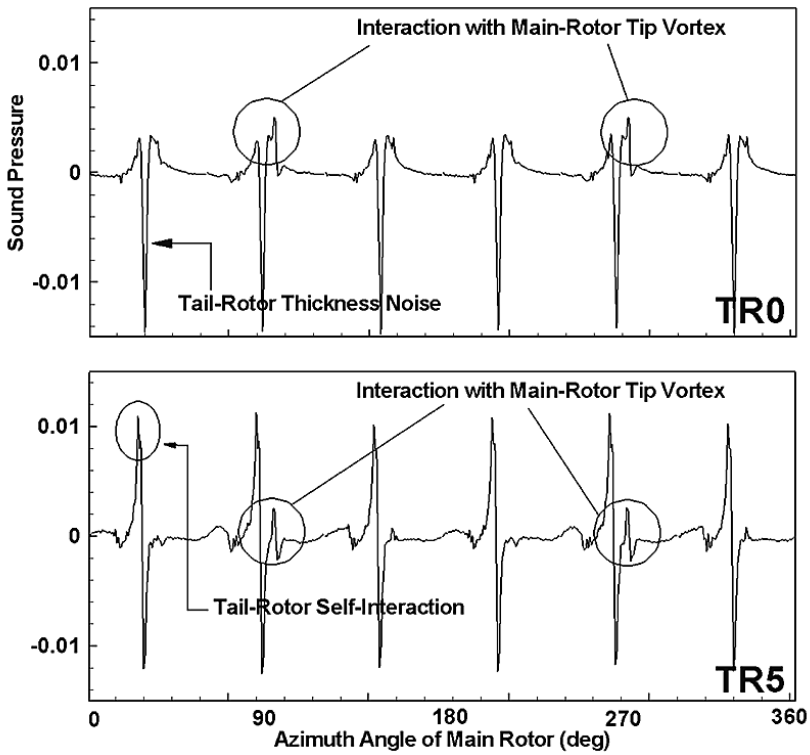

Fig. 21 BVI sound pressure of tail rotor in forward flight (ψ = 205°, φ = –25°, r/R = 1000).

present study is an order of magnitude less than the most severe main-rotor BVI noise, it is worth capturing the distinct peak from the tail rotor for both self-interaction and interaction with the main-rotor tip vortex using the present CFD method.

3.4 Forward Flight in Different Flight Condition

The effect of different forward flight condition is simulated to compare the tail-rotor interaction noise with the tip vortex of main-rotor in higher advancing ratio. As mentioned in the introduction, the effect of main rotor tip vortex onto tail rotor is dependent on the forward flight condition when other conditions such as the location of tail rotor and tail rotor rotating condition are fixed.

Figure 22 shows the comparison of vorticity iso-surface for different flight condition. Interval distance between two tip vortices of main-rotor, which is marked as ***d***, is totally dependent on the flight condition, i.e. advancing ratio. Figure 23 shows the comparison of pressure history at one point (as shown in Fig. 16) of both main-rotor and tail-rotor for one revolution of main-rotor for different flight condition. The phenomena of two interactions (as shown as two negative peaks added to the six periodic oscillations) between tip vortices from main rotor and tail rotor during one revolution of main rotor doesn't change, which is a matter of course when considering (1) relative rotational speed between

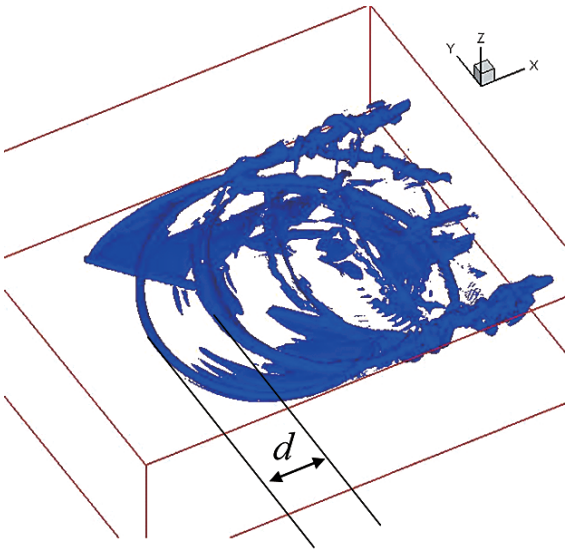

(a) μ=0.164,θ_T= 0˚

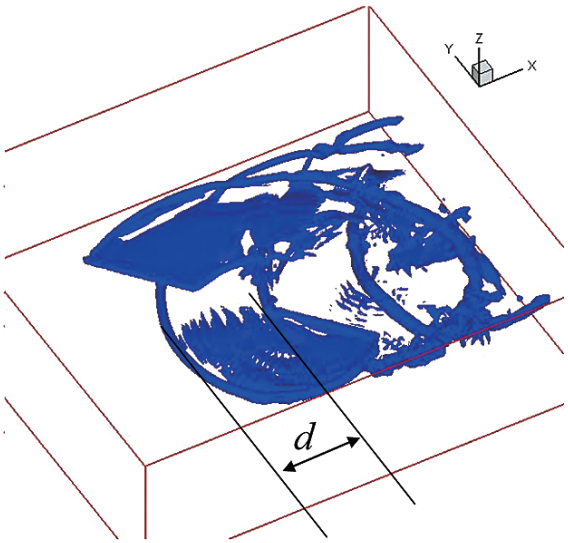

(b) μ=0.224, θ_T = 0˚

Fig. 22 Comparison of vorticity iso–surface for different flight condition

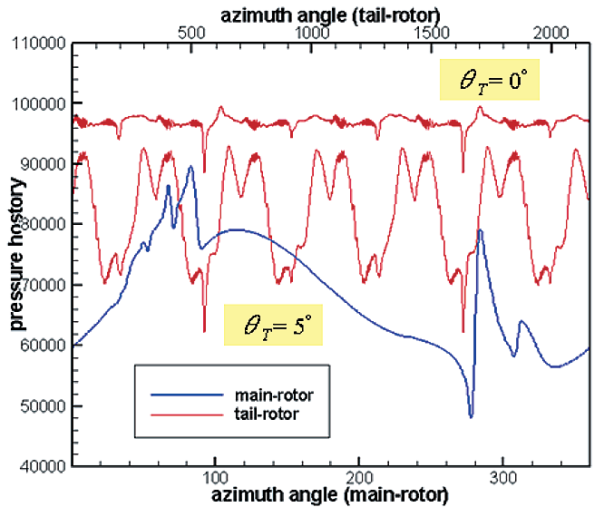

(a) μ=0.164, *TPP*=3˚, θ_T= 0, 5˚

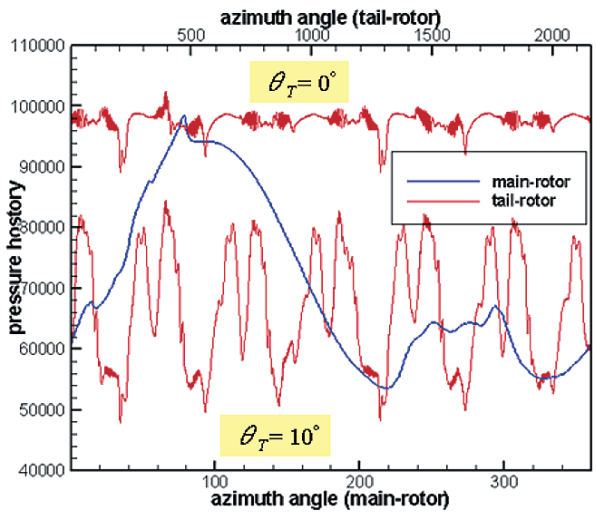

(b) μ=0.224, *TPP*=-2˚, θ_T= 0, 10˚

Fig. 23 Comparison of pressure history at one point for one revolution of main-rotor & tail-rotor

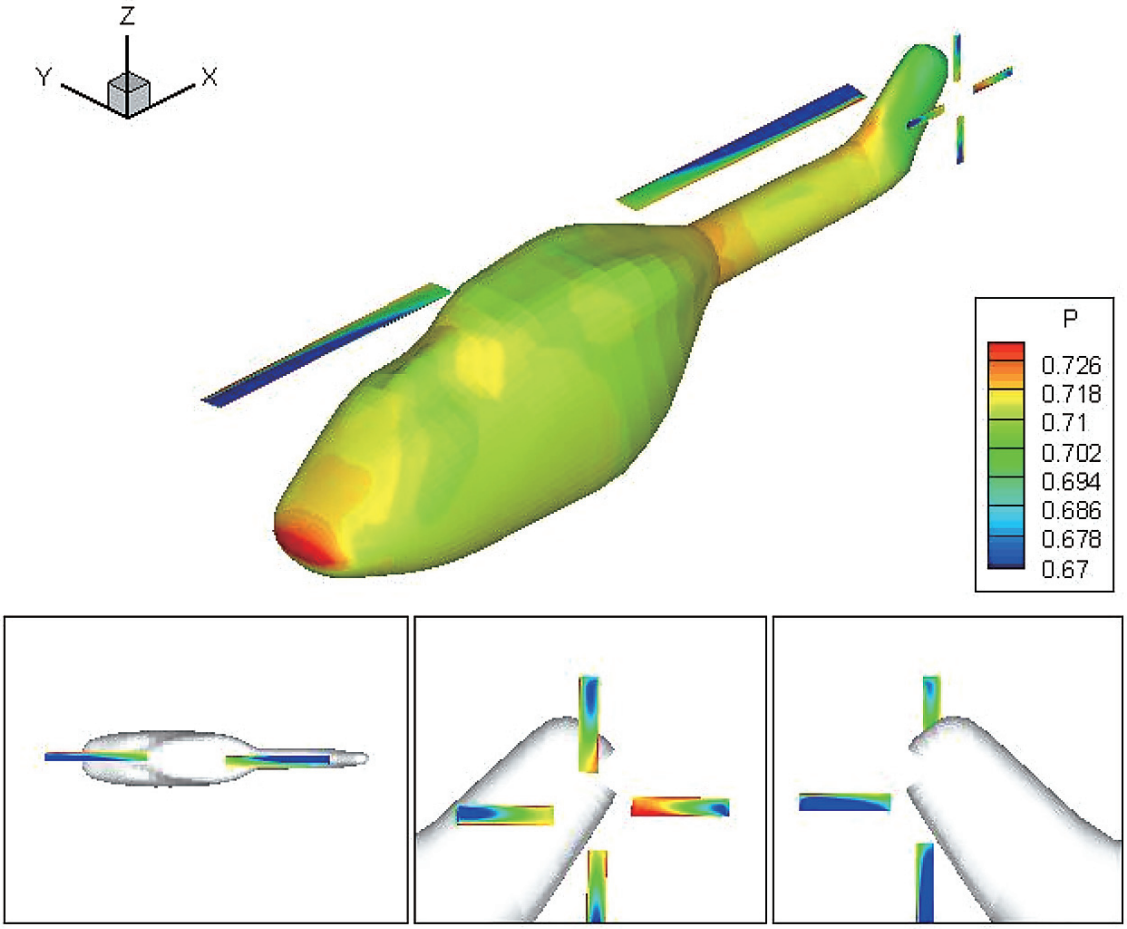

Fig. 24 Preliminary calculation for full helicopter

main rotor and tail rotor, and (2) numbers of blades for main rotor and tail rotor. But the interaction positions change according to the flight conditions, as shown in the figure.

Figure 24 shows the surface pressure of the preliminary calculation for full helicopter when including a fuselage. Effect of fuselage on tail rotor will be studied in the future research.

4. CONCLUSIONS

A simulation method for full helicopter configuration is constructed by combining an unsteady Euler code with an acoustic code based on the Ffowcs-Williams and Hawkings formulation. Flowfield and helicopter noise in hover and forward flight are calculated to understand the mutual interaction between the main rotor and tail rotor. The following conclusions were obtained.

(1) The calculated waveform of main-rotor BVI noise clearly shows distinct peaks suggesting that the present method can capture BVI phenomena for both the main rotor and tail rotor.

(2) In the hovering flight calculation, the tail rotor disturbs the surface pressure of the main rotor because the tail-rotor tip vortex is dragged by the induced main-rotor tip vortex flow. The detailed flow patterns are well described.

(3) In forward-flight calculation, the tail-rotor interaction characteristics are well captured including tail rotor self-interaction and interaction between the tail rotor and the main rotor tip vortices. The self-interaction noise is comparable to the thickness noise.

REFERENCES

1) T. F. Brook, J. R. Jolly, M. A. Marcolini, Helicopter main-rotor noise, NASA Technical Paper 2825, 1988.

2) White, R. P. Jr., The status of rotor noise technology: One man's opinion, NASA Center for AeroSpace Information (CASI), 1978.

3) Chou, S. -T., A study of rotor broadband noise mechanism and helicopter tail rotor noise, NASA-CR-177565, 1990.

4) Martin, R. M., Acoustic test of a model rotor and tail rotor: Results for the isolated rotor and combined configuration, NASA-TM-101550, 1989.

5) Balch, D. T., Lombardi, J., Experimental study of main rotor tip geometry and tail rotor interaction in hover. Volume 1. Text and figures, NASA-CR-177336-VOL-1, 1985.
6) Balch, D. T., Lombardi, J., Experimental study of main rotor tip geometry and tail rotor interaction in hover. Volume 2. Run log and tabulated data, NASA-CR-177336-VOL-2, 1985.
7) Leverton, J. W., Pollard, J. S., and Wills, C. R., Main rotor wake/tail rotor interaction, Vertica, Vol.1, pp. 213–221, 1977.
8) George, A. R. and Chou, S. -T., Helicopter tail rotor noise analysis, NASA-CR-176829, 1986
9) George, A. R. and Chou, S. -T., Helicopter tail rotor blade-vortex interaction noise, NASA-CR-183178, 1987.
10) Ahmadi, A. R., An experimental investigation of the chopping of helicopter main rotor tip vortices by the tail rotor, NASA-CR-177338, 1984.
11) Aoyama, T., Yang, C., Kondo, N., and Saito, S., "Fundamental CFD Analysis on Main rotor/Tail rotor Interaction Noise of Helicopters", Theoretical and Applied Mechanics Japan, Vol. 53, pp. 215–220, October, 2004.
12) Kondo, N., Aoyama, T., and Saito, S., "Calculation of Helicopter Rotor-Fuselage Interaction by Moving Overlapped Grid Method", The 5th Asian Computaional Fluid Dynamics, Busan, Korea, June 30-July 3, 2003.
13) Boxwell, D. A., Schmitz, F.H., Splettstoesser, W.R. and Schults, K.J., Helicopter model rotor-blade vortex interaction impulsive noise: scalability and parametric variations, J. of American Helicopter society, Vol. 32, No.1 pp. 3–12, 1987.
14) Ochi, A., Shima, E., Aoyama, T., and Saito, S., A numerical simulation of flow around rotor blades using overlapped grid, Proceedings of the 15th NAL Symposium on Aircraft Computational Aerodynamics (NAL SP-37), pp. 211–216, Tokyo, Japan, Jul 1997, acoustics Conference, AIAA 86–1877, 1986.
15) Roe, P. L., Approximate Riemann solvers, parameter vectors, and different schemes, Journal of Computational Physics, Vol.43, pp. 357–372, 1981.
16) Aoyama, T., Kawachi, K., Saito, S. and Kamio, J. Unsteady analysis of transonic helicopter rotor noise, 19th European Rotorcraft Forum, 1993.
17) Yamamoto, S. and Daiguji, H., Higher-order-accurate upwind schemes for solving the compressible Euler and Navier-Stokes equations, Journal of Computers & Fluids, 22, pp. 259–270, 1993.
18) Shima, E. and Jounouchi, T., Role of CFD in aeronautical engineering (No.14) -AUSM type upwind schemes-, Proceedings of the 14th NAL Symposium on Aircraft Computational Aero-dynamics (NAL SP-34), pp. 7–12, Tokyo, Japan, Jul 1996.
19) Farassat, F., Theory of noise generation from moving bodies with an application to helicopter rotors, NASA TR R 451, 1975.
20) Brentner, K. S., Helicopter rotor noise prediction: Background, current status, and future direction, Seminar in University Tennessee Space Institute, Chattanooga, Tennessee, 1997.
21) Johnson, W., Rotorcraft aerodynamics applications of comprehensive analysis, Heli-Japan 98, Paper No.S5, Gifu, Japan, April 1998.
22) Heyson, Harry H., Linearized Theory of Wind-Tunnel Jet-Boundary Corrections and Ground Effect for VTOLSTOL Aircraft. NASA TR R-124, 1962.
23) Strawn, R. C., Duque, E. P. N., and Ahmad, J., Rotorcraft Aeroacoustics Computations with Overset-Grid CFD Methods, Journal of the American Helicopter Society, Vol. 44, (2), pp. 132–140, 1999.